analytical chemistry

pubs.acs.org/ac Article

Compressed Sensing Image Reconstruction of Scanning Electrochemical Microscopy Measurements Carried Out at Ultrahigh Scan Speeds Using Continuous Line Probes

Anna E. Dorfi,[#] Jingkai Yan,[#] John Wright,[*] and Daniel V. Esposito[*]

Cite This: *Anal. Chem.* 2021, 93, 12574−12581 Read Online

ACCESS | Metrics & More | Article Recommendations | Supporting Information

ABSTRACT: Previous studies on scanning electrochemical microscopy (SECM) imaging with nonlocal continuous line probes (CLPs) have demonstrated the ability to increase areal imaging rates by an order of magnitude compared to SECM based on conventional ultramicroelectrode (UME) disk electrodes. Increasing the linear scan speed of the CLP during imaging presents an opportunity to increase imaging rates even further but results in a significant deterioration in image quality due to transport processes in the liquid electrolyte. Here, we show that compressed sensing (CS) postprocessing can be successfully applied to CLP-based SECM measurements to reconstruct images with minimal distortion at probe scan rates greatly exceeding the conventional SECM "speed limit". By systematically evaluating the image quality of images generated by adaptable postprocessing CS methods for CLP-SECM data collected at varying scan rates, this work establishes a new upper bound for CLP scan rates. While conventional SECM imaging typically uses probe scan speeds characterized by Péclet numbers (Pe) < 1, this study shows that CS postprocessing methods can allow for an accurate image reconstruction for Pe approaching 5, corresponding to an order of magnitude increase in the maximum probe scan speed. This upper limit corresponds to the onset of chaotic convective flows within the electrolyte for the probes investigated in this work, highlighting the importance of considering hydrodynamics in the design of fast-scanning probes.

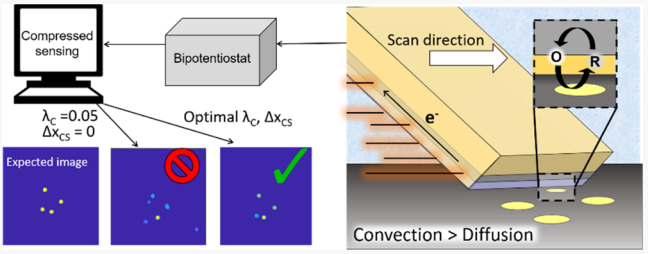

1. INTRODUCTION

A major research push in the development and use of scanning electrochemical microscopy (SECM) techniques is in breaking the probe's "speed limit" to enable more efficient imaging of large areas, higher sample throughput, and/or video-rate imaging of dynamic systems.[1,2] This "speed limit" represents a maximum probe scan speed beyond which intolerable levels of image distortion and/or loss of resolution occur. This limit is generally based on either hardware limitations of the microscope or physical limitations of the electrochemical phenomena associated with a particular SECM imaging mode.[1] One common physical limitation in SECM is the diffusion of electroactive species between the SECM probe and substrate, which tends to be characterized by slow time constants and often becomes problematic for micron or larger probes.[1,3] However, other factors like probe-induced convection within the electrolyte can also become a leading contributor to distortion at high scan speeds.[4,5] Regardless of the origin of a probe's scan limit, it is desirable to be able to evaluate the speed limit and assess how that limit changes for different probe geometries and SECM imaging modalities.

SECM researchers have been able to increase imaging rates through a variety of approaches, including but not limited to (i) using more efficient probe scan patterns,[1] (ii) parallel imaging with multiple sensing elements integrated into brush-like probes;[6−8] (iii) using nonlocal probes combined with compressed sensing (CS) image reconstruction;[9,10] (iv) manufacturing higher resolution nanoprobes;[11−13] (v) interpreting fast scanning SECM measurements carried out at varied scan rates with finite element simulations;[14−16] and (vi) employing postprocessing methods to correct for distortion.[17−20] Postprocessing methods are especially attractive for overcoming image distortion at high scan rates since they do not necessarily require any changes to the microscope hardware. In general, previous work on these methods have taken approaches including deconvolution using the inverse response[17,18] and image deblurring algorithms based on Laplacian and Gaussian filtering.[20] Direct input of knowledge about the physical and chemical phenomena that are the root causes of image distortion also presents opportunities to improve postprocessing algorithms.[5]

Received: May 3, 2021
Accepted: August 18, 2021
Published: September 8, 2021

Downloaded via COLUMBIA UNIV on December 9, 2021 at 13:09:55 (UTC).
See https://pubs.acs.org/sharingguidelines for options on how to legitimately share published articles.

© 2021 American Chemical Society

https://doi.org/10.1021/acs.analchem.1c01869
Anal. Chem. 2021, 93, 12574−12581

Our groups have been particularly interested in increasing SECM imaging rates by using CS image reconstruction to generate images from SECM measurements taken with nonlocal probes that contain at least one nano- or microscopic dimension and one macroscopic dimension.[9,10] While the microscopic dimension of the probe is required to achieve high imaging resolution, the macroscopic dimension of the sensing element enables simultaneous electrochemical interactions to occur at many points on the sample surface, providing opportunities to greatly increase the total amount of information that is obtained at any given moment.[9] So far, our efforts have focused on scanning band electrodes referred to as continuous line probe (CLPs) as nonlocal probes, with past work demonstrating the ability of CLP-based SECM (CLP-SECM) combined with CS to be capable of increasing areal imaging rates by at least an order of magnitude compared to conventional micron-scale ultramicroelectrodes (UMEs).[9,10] As shown in the left side of Figure 1, the CLP is a nonlocal probe consisting of a continuous band electrode (i.e., sensing element) that is sandwiched in between two insulating layers. The nonlocal nature of the CLP is in contrast to the conventional UME (right side of Figure 1), which often takes the form of a microscopic electroactive disk electrode encased in an insulating material like glass. This conventional UME can be considered a "point probe" that measures electrochemical signal *locally* at the disk. For both types of electrodes, Figure 1 illustrates a simplified visualization of SECM imaging in feedback mode whereby the redox species generated at the substrate is consumed at the probe and vice versa. During imaging, the CLP measures the aggregate intensity of the electrochemical signal along the entire length of the band electrode. From the perspective of image processing, imaging with a UME is equivalent to sampling an image in a laborious pixel-by-pixel manner, while CLP imaging effectively takes a line integral of the target image at the given CLP position. From aggregate signal intensities measured with a CLP at various positions on a sample surface, it is necessary to apply appropriate postprocessing steps to reconstruct the target 2D image using CS.[9]

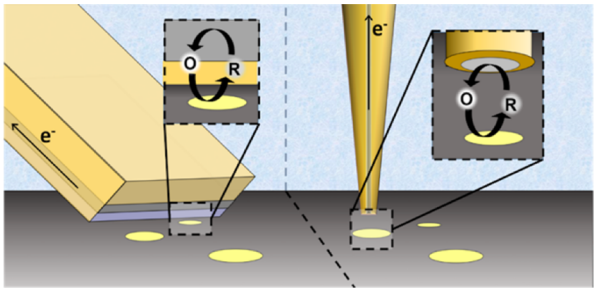

Figure 1. Geometry of a continuous line probe (CLP) (left image) and a conventional ultramicroelectrode (UME) (right image) used for scanning electrochemical microscopy (SECM) imaging of electroactive objects (yellow disks) on an inert or insulating substrate (dark gray surface).

CS is a relatively new field in signal processing that provides new approaches to the classic problem of signal sampling and reconstruction. CS has been widely applied in various fields of imaging, including magnetic resonance imaging (MRI),[21,22] radar imaging,[23] holography,[24] and more. In the classic Shannon–Nyquist sampling theory,[25] there is a lower bound on the sampling rate required to achieve a desired resolution. However, CS takes advantage of additional properties of the target signal to enable a perfect reconstruction of signals with much fewer measurements than predicted by the classic sampling theory.[26,27] One property or characteristic of a target image that is particularly important in CS is its sparsity. An image is considered sparse if it contains a small number of features of interest relative to the total number of image pixels associated with a target image area and desired resolution. In SECM imaging, sample surfaces characterized by a relatively small number of electroactive objects (e.g., nanoparticles, defects, and edges) scattered over large areas can be considered to have a high degree of sparsity and therefore can be addressed by CS reconstruction methods. Such samples that are characterized by a high degree of sparsity are often extremely time consuming to image with conventional SECM, for which the exhaustive pixel-by-pixel scanning approach with a conventional UME "point probe" is highly inefficient. This is especially true when the size of the sparsely distributed features is very small compared to the dimension of the total area being imaged.[9]

In previous proof-of-principle demonstrations of CLP-SECM imaging, CLP scan speeds were kept at or below the maximum speeds typically employed in conventional UME-based SECM (≈2−3 probe radii per second). At these speeds, the characteristic time constant associated with the probe/substrate interaction is smaller than the time constant associated with the probe residence time in a given pixel, ensuring minimal signal distortion and obviating the need for extra postprocessing beyond the groundwork compressed sensing developed in our previous studies.[9,10] However, SECM measurements carried out at faster scan rates experience significant distortion in the imaged features (e.g., shifts in location and asymmetric line shapes) and deviation in their signal intensities from those expected under steady-state diffusion-controlled operation.[1,4] Understanding the underlying physical basis for these distortions is extremely important for incorporating accurate models for the interaction between the probe and the sample into image reconstruction postprocessing. Toward this end, we recently employed *in situ* colorimetric imaging to visualize the "plumes" of redox species during CLP-SECM line scan measurements to better understand how probe hydrodynamics changed as a function of probe scan rate and how those changes translated to distortions in the SECM measurements.[5] Consistent with a previous study by Combellas et al. looking at the hydrodynamics of conventional UMEs,[4] our work identified different transport regimes for CLPs that could be classified based on the Péclet (*Pe*) number of the system, which is a dimensionless number representing the ratio of convective to diffusive transport rates in a system.[28] For a scanning SECM probe, *Pe* may be defined as:[4]

$$Pe = \frac{\text{rate of convection}}{\text{rate of diffusion}} = \frac{v_p \cdot d}{D_i} \quad (1)$$

where v_p is the probe scan rate relative to the substrate, d is the probe−substrate separation distance, and D_i is the diffusion coefficient for species i. For the CLP geometry shown in Figure 1, d is taken to be the average distance between the CLP sensing element and the substrate along a line that is perpendicular to the substrate. Our previous study identified three transport regimes that corresponded to ranges of v_p and *Pe* and correlated strongly with trends in distortion character-

https://doi.org/10.1021/acs.analchem.1c01869
Anal. Chem. 2021, 93, 12574−12581

istics of CLP line scan measurements. At low probe scan speeds corresponding to $Pe < 1$, the time constant for diffusion of species between the substrate and probe is smaller than that associated with the probe scanning across the electroactive feature of interest, leading to minimal feature distortion and no shift between the probe location associated with peak current signal and the physical location of the electroactive object (Δx). At intermediate scan speeds corresponding to $1 < Pe < 3$, species diffusion begins to limit the measurement, resulting in increasingly pronounced feature distortions and nonzero Δx consistent with a well-defined Couette-type sheer flow created in the fluid by the scanning probe. In the third regime, corresponding to $Pe > 3$, peak distortions become highly pronounced, seen in the form of significant increases in the asymmetry and full width at half-maximum (FWHM) of peaks measured during line scans over isolated disk electrodes. As seen by *in situ* colorimetric imaging of redox species plumes, this third regime was characterized by a more complex flow behavior that could not be easily used to describe peak shifts.

In the current study, we leverage the recent understanding of the different transport regimes in CLP-SECM line scans to help guide the development of a new CS algorithm for reconstructing 2D SECM images from CLP line scans carried out at probe scan speeds characterized by $Pe > 1$. This work focuses on a sample containing four electroactive Pt disks and demonstrates the ability of using CS methods to correct for distortion and enable SECM imaging rates at scan speeds that greatly exceed the conventional SECM "speed limit".

2. EXPERIMENTAL SECTION

2.1. Materials. All electrochemical measurements were carried out in aqueous solutions prepared from 18.2 MΩ-cm deionized water. Concentrated sulfuric acid (Certified ACS plus, Fischer Scientific), sodium sulfate (ACS reagent grade, Sigma Aldrich), potassium hexacyanoferrate(II) trihydrate (ACS reagent grade, Sigma Aldrich), and sodium chloride (ACS reagent grade, Sigma Aldrich) were used as received without further purification. A platinum wire (Alfa Aesar, 99.95% metals basis, 50 μm diameter) served as the counterelectrode, while a miniature Ag/AgCl electrode (EDAQ, 3 M KCl) was used as the reference electrode.

2.2. Fabrication of CLPs. Band microelectrodes were fabricated in a similar manner to what was described by Wehmeyer et al.[29] A polycarbonate sheet (TapPlastics, 0.02 in., ≈500 μm thick), Pt foil (Alfa Aesar, 99.999% purity), and Kapton tape (1 Mil, 1/2" × 36 yards, Uline) were used as the materials of construction for the CLP. First, the 25 μm thick Pt foil (Fischer Scientific, 99.99% metals basis) was sealed to an insulating polycarbonate substrate using a two-part 5 min epoxy (JB Weld). To ensure a good seal between the Pt and the PC substrate, a vice was used to apply uniform pressure overnight while the epoxy cured. The top surface of the Pt foil was electrically insulated using the Kapton tape (thickness ≈ 70 μm). The thickness of the Kapton tape is very important because it serves as the insulating layer that is in contact with the substrate during measurements and therefore determines the average separation distance between the substrate and Pt layer. The CLP was cut to dimensions of 4.75 × 15 mm. The edge of the CLP was exposed by cutting the end with a microtome and polishing with a home-built polishing system employing a 1 μm alumina lapping paper (McMaster-Carr), followed by polishing with a slurry of 0.05 μm gamma alumina powder on a Microcloth polishing pad (CHI Instruments).

2.3. Fabrication of Substrates. The disk electrode patterns were prepared by evaporating metals (Ti as an adhesion layer and Pt as the electrocatalyst) onto degenerately doped p + Si wafers through a shadow mask via electron beam deposition (High Vacuum Angstrom EvoVac, 1×10^{-8} Torr base pressure). Titanium and Pt were deposited sequentially without having to break the vacuum. The Pt/Ti disk electrodes had diameters of 150 μm, and the thicknesses of the Ti and Pt layers were set to 2 and 50 nm, respectively. The layer thickness was monitored during the deposition using a quartz crystal thickness monitor. Electrical connection to the back of the p^+Si was made by the use of a silver (Ag) conductive paint (SPI Supplies). When the substrate is clamped into the electrochemical cell for imaging, the sample back contact is physically pressed into a piece of copper foil tape (3M Copper Conductive Tapes) placed on the base of the cell.

2.4. SECM Measurements. The reversible hydrogen redox couple was investigated in all experimental studies, and imaging was done in the substrate generation/tip collection (SG/TC) SECM mode. The electrolyte used was 5 mM H_2SO_4 and 100 mM Na_2SO_4 titrated to pH 5 using 100 mM NaOH. The substrate potential during measurements was held at −0.8 V AgAgCl (−0.30 V vs RHE), and the probe potential was held at 0.9 V AgAgCl (1.4 V vs RHE). A home-built CLP-SECM microscope was used to carry out the measurements as previously described in detail.[10] Briefly, the procedure for carrying out SECM measurements was as follows: First, the CLP probe height and angle with respect to the substrate (θ_{CLP}, see Figure 1a,b) is fixed based on an approach curve that is measured using a procedure similar to that used in setting up a constant height imaging acquisition with a conventional SECM instrument. In this work, all measurements were conducted with $\theta_{CLP} \approx 45°$, which corresponds to an average vertical distance between the substrate and band electrode of 60 μm. After establishing the desired θ_{CLP}, the sample area to be imaged is aligned such that (i) the center of the target imaging area coincides with the midpoint of the CLP, (ii) the distance from the CLP band electrode to the center of the imaging area is set to half of the desired scan length, and (iii) the sample substrate is rotated such that the angle of the CLP scan direction with respect to the substrate ("scan angle", θ_S) is set to the user-specified value. Eight line scans were then carried out for each of the different scan angles at a user-defined probe scan speed (ν_p). The definition of θ_S is illustrated in Figure S1a, and an example of the line scan measurements at 121 μm s^{-1} of the four-disk sample used for most of this study is provided in Supplementary Information Figure S1.

2.5. Compressed Sensing Algorithm. The CS reconstruction procedure consists of solving a mathematical optimization problem, which will be described in detail later. The optimization problem is solved using the *clpsecm_imaging* MATLAB package.[30] The package takes as input the scan time (converted to position based on the scan speed) and the corresponding measured electrochemical current and produces as output the reconstructed image. At the core of the package is an algorithmic solver for the specific optimization problem of CLP-SECM, which solves the problem via an iterative algorithm named "Reweighted Inertial Proximal Alternating Linearized Minimization" (Reweighted iPALM).[31]

https://doi.org/10.1021/acs.analchem.1c01869
Anal. Chem. 2021, 93, 12574−12581

3. RESULTS AND DISCUSSION

3.1. Relationships between Probe Scan Speed and SECM Distortion Characteristics. Probe scan speeds typically used in conventional SECM coincide to $Pe < 1$, for which diffusion is the primary mode of species transport and the current passing between the probe and substrate can achieve steady-state or pseudo-steady-state characteristics.[17,32] Under these conditions, the concentration profile of a redox species generated by an electroactive object will be symmetric about that object and should remain relatively unperturbed as a probe passes through it, as seen experimentally[5] and illustrated schematically in Figure 2a. At fast scan speeds where

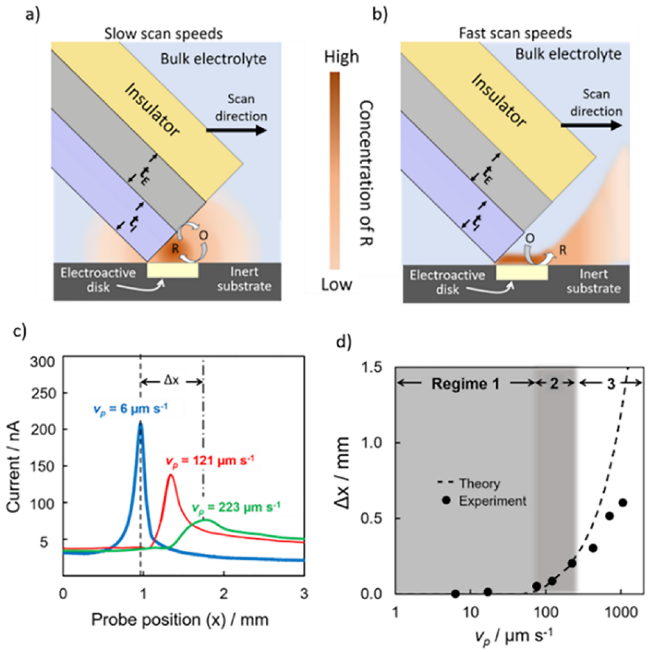

Figure 2. Schematic side-views of a CLP scanning from left to right across an electroactive disk electrode while imaging in substrate generation/tip collection (SG/TC) mode using (a) slow and (b) fast scan speeds that lead to significant differences in the redox species concentration profiles as described in the text. (c) CLP line scan measurements recorded with a t_E = 25 μm Pt-based CP across a 150 μm diameter disk electrode at three different probe scan rates. Measurements were carried out in 5 mM H_2SO_4 and 0.1 M Na_2SO_4 in SG/TC mode based on the reversible hydrogen reaction with the substrate held at −0.8 V vs Ag|AgCl and the CLP potential held at 0.9 V vs Ag|AgCl. The vertical dashed line in (c) corresponds to the physical location of the center of the disk electrode. (d) Comparison of the experimentally observed peak shift (Δx) to that predicted from theory as a function of probe scan speed (v_p). Also indicated in subfigure (d) are three different operational regimes that can be classified according to transport characteristics of the system.

convection becomes the dominant mode of transport and $Pe \gg 1$, the recorded signal deviates from the steady-state signal, making the quantitative understanding of the local kinetics or properties of the surface more difficult. Additionally, fluid flow in the vicinity of the probe can greatly alter the spatiotemporal characteristics of the concentration profiles of redox species during the scan. One example of this, consistent with experimental observations,[5] is illustrated schematically in Figure 2b. Under fast scan rates, the angled CLP placed in contact with the sample surface has the effect of "pushing" the "plume" of substrate-generated redox species in the same direction as the movement of the probe.

A distortion in the concentration profiles of redox species from their steady-state profiles can be expected to lead to a significant distortion in the electrochemical line scan measurements that are recorded as the CLP as it passes over the electroactive object. To systematically view the impacts of probe scan speed on distortion effects, CLP-SECM line scans were performed by scanning a CLP with a t_E = 25 μm thick sensing element over an isolated 150 μm diameter Pt disk electrode. These SECM measurements were carried out in substrate generation/tip collection (SG/TC) mode, where hydrogen (H_2) was evolved from the disk electrode and subsequently oxidized at the CLP sensing element during operation in 5 mM H_2SO_4 and 0.1 M Na_2SO_4. Line scans were carried out with scan speeds ranging from 6 to 1000 μm s^{-1}, with the results of three representative scans at varying scan speeds shown in Figure 2c. As expected, the lines scan measured at the lowest scan speed (6 μm s^{-1}, corresponding to Pe = 0.07) exhibits peak current at a probe location that coincides exactly with the physical location of the center of the disk electrode (i.e., Δx = 0 mm). This line scan is also characterized by a relatively narrow FWHM and low degree of asymmetry, consistent with redox species concentration profiles that remain unperturbed and symmetric about the disk electrode as the probe passes over it. However, several changes in the shape of the line scan profile emerge at faster v_p. When v_p increases to 121 μm s^{-1} (corresponding to Pe = 1.42), there is a distinct and significant peak shift that is accompanied by a decrease in the peak signal intensity, an increase in its FWHM, and an emergence of a noticeable tail extending to probe positions that are well downstream of the disk electrode. These effects become even more pronounced for the line scan measured at v_p = 223 μm s^{-1} (corresponding to Pe = 2.62), which also exhibits the emergence of subtle secondary peaks at large Δx. A comparison of the dependence of Δx on scan rate across the full rate of v_p values is shown in Figure 2d along with the expected theoretical value of Δx according to the model described in our previous work.[5] By comparing the experimental and theoretical values of Δx, we can identify the three aforementioned operational regimes. In regime 1, corresponding to $Pe < 1$, the time constant for species diffusion (τ_D) is less than the probe residence time across the disk electrode (τ_p), leading to $\Delta x \approx 0$ mm. As v_p increases and the opposite becomes true (i.e., $\tau_D > \tau_p$), nonzero Δx values are observed. In regime 2, corresponding to $1 < Pe < 3$, excellent agreement is observed between the experimental and theoretical Δx. At Pe larger than 3, the theoretical value of Δx greatly exceeds that observed experimentally. We have ascribed this disagreement in regime 3 to the emergence of convective cells within the vicinity of the probe, which greatly enhance species transport within the electrolyte compared to diffusion such that Δx is much less than expected.[5]

3.2. Compressed Sensing (CS) Theory. Having established the basic relationships between feature distortion characteristics like Δx and probe scan speed, we present the motivating question for this study: how does increasing Δx, peak FWHM, and peak asymmetry at high probe scan speeds (i.e., high Pe) affect the ability of CS to accurately reconstruct SECM images from CLP line scans? To understand these limits, it is necessary to discuss the basic framework that underlies CS image reconstruction algorithms. In short, CS reconstruction solves an optimization problem that essentially

https://doi.org/10.1021/acs.analchem.1c01869
Anal. Chem. 2021, 93, 12574−12581

searches for a target image X that (i) agrees with the observed measurements and (ii) satisfies structural assumptions such as sparsity. These two desiderata are encoded in an objective function $f(X) = L_1(X) + \lambda L_2(X)$ that is minimized, where X stands for the raw data input to the reconstruction algorithm, $L_1(X)$ is a measure of the misfit between X and the observed measurements, $L_2(X)$ is a measure of how nonsparse X is, and the sparsity coefficient λ trades off between these two terms of data fidelity and sparsity. Smaller values of λ put relatively more weight on the first term $L_1(X)$, and hence, the minimization of the objective function more strongly promotes solutions that maintain high fidelity to the observed measurements, which is desirable in experimental data sets characterized by a lower signal-to-noise ratio. Conversely, larger values of λ put more weight on $L_2(X)$, and the minimization procedure more strongly promotes accuracy of the structural properties of the reconstructed image (e.g., sparsity) and places a lower emphasis on achieving maximum fidelity to the observed measurements. The appropriate choice of λ depends on the signal-to-noise ratio of the measurements and the degree to which the sample is sparse. In our original papers on this CS algorithm,[9,33] we proposed that $\lambda = \lambda_c M$, where $\lambda_c = 0.05$ and M is the value of the pixel with the highest signal intensity in the back-projected image, which is the image produced when compiled line scans recorded by scanning the CLP across the image area at different scan angles are projected onto each other, as described in more detail elsewhere[9].

Here the notion of "signal-to-noise ratio" refers to the fact that non-idealities in the measurement become more pronounced at high scan speeds. The non-idealities consist of two main factors: (1) the point spread function becomes distorted from our model at high speeds, and (2) high scan speeds worsen the spatial resolution of the measurement, making it hard to reconstruct two disks located very close together. Random noise from the environment and equipment may also contribute to worsening signal-to-noise ratio in the electroanalytical measurements but was not noticeably impacted by scan rate over the range of scan rates investigated in this work as evidenced by the relatively smooth line scan measurements shown in Figure 2c.

The measurements in Figure 2c exhibit the following effects that degrade the quality of CS reconstruction: as the scan speed increases, the peak signal shifts in the same direction that the probe is scanned (i.e., to the right in Figure 2c), decreases in height, increases in FWHM, and experiences increased asymmetry due to the development of a "tail" at probe locations downstream of the disk. In the CS reconstruction, the data fidelity term $L_1(X)$ makes use of a predefined point spread function, which is the response of the line probe to a single point. In previously employed CS reconstruction algorithms,[9,33] the point spread function that is characteristic of the probe/substrate interaction was assumed to be centered over the electroactive feature from which signal originates such that $\Delta x = 0$ mm. The decrease in peak height also impacts the quality of reconstruction: measurements with a smaller peak tend to have a lower effective signal-to-noise ratio. Moreover, based on our previous analysis of CLP line scans recorded at fast scan speeds,[5] we expect to encounter more noise in this scenario, meaning that accurate reconstruction can be expected to require a larger λ.

3.3. Image Reconstruction at Fast Scan Rates Using Traditional CS Algorithm. As a baseline test of the ability of CS to reconstruct CLP-SECM images at fast scan rates, we carried out a series of CLP line scan measurements over a sample containing four 150 μm diameter electroactive Pt disk electrodes.

A top view photo of this sample is shown in Figure 3a. Line scan measurements were carried out using a wide range of CLP

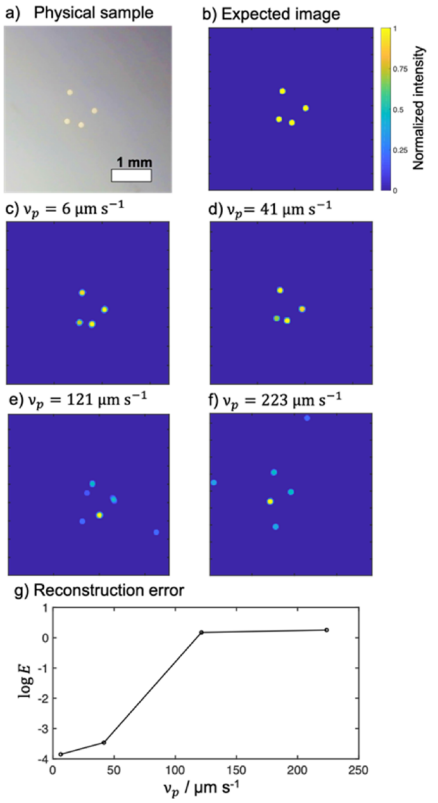

Figure 3. (a) Photograph of sample containing four Pt disks, each with 150 μm diameter, deposited onto an inert p + Si(100) wafer. (b) Expected SECM image based on the physical location of the Pt disks shown in (a). SECM images reconstructed by conventional compressed sensing (CS) algorithm using CLP line scan data that were recorded at scan rates of (c) 6 μm s^{-1}, (d) 41 μm s^{-1}, (e) 121 μm s^{-1}, and (f) 224 μm s^{-1}. All SECM measurements were carried out in SG/TC mode as described in the Figure 2 caption. (g) Reconstruction error (E) at different scan rates. The scale bar shown in (a) also applies to figures (b–f).

scan speeds: 6, 41, 121, 224, and 425 μm s^{-1}. For each scan speed, eight scans were taken at different angles (0, 20, 40, 60, 80, 100, 120, and 140°) across the sample to obtain complementary information about the sample from each scan. First, we applied conventional CS reconstruction algorithms[9,33] to generate the images shown in Figure 3c–f using a default choice of $\lambda_c = 0.05$ and no shift compensation (i.e., $\Delta x = 0$). For the slowest scan speed, $v_p = 6$ μm s^{-1}, Figure 3c shows that the conventional CS algorithm does an excellent job of recovering an image that closely resembles the expected target image (Figure 3b). The algorithm is still able to accurately reconstruct the image when v_p increases to 41 μm s^{-1} ($Pe = 0.48$), although subtle variations in the location and intensity of the reconstructed disks begin to appear. As v_p increases further to 121 μm s^{-1} ($Pe = 1.42$) or 223 μm s^{-1} ($Pe = 2.62$), the conventional CS algorithm becomes incapable of accurately reconstructing an image that resembles the target image. In particular, the two disks at the bottom-left suffer

https://doi.org/10.1021/acs.analchem.1c01869
Anal. Chem. 2021, 93, 12574−12581

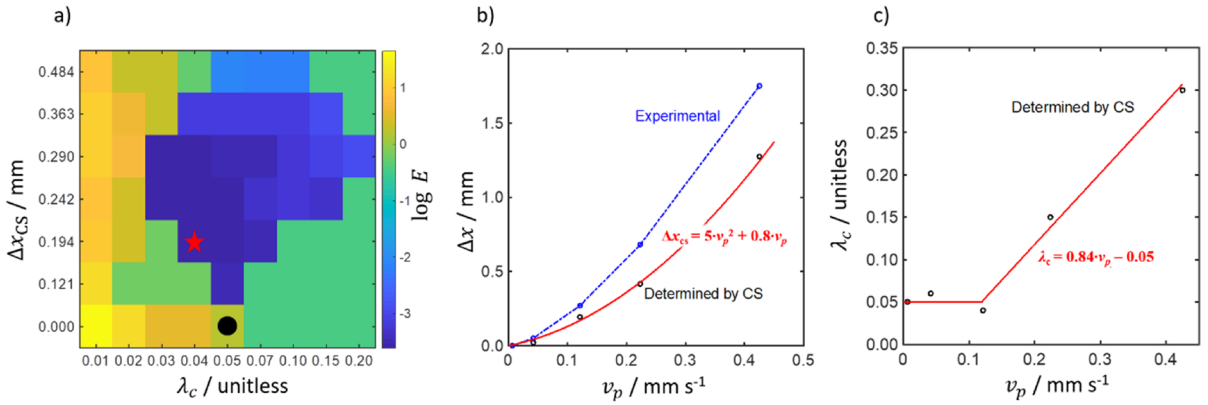

Figure 4. (a) Color map showing how CS reconstruction error changes as a function of λ_c and Δx for CLP-SECM line scan data recorded for the four-disk sample shown in (a) at a probe scan rate v_p = 121 μm s^{-1}. Reconstructions were carried out using eight line scans recorded at varied scan angles. The black dot in (a) indicates the conditions used for the conventional CS algorithm, while the red star marks the combination of λ_c and Δx that resulted in the lowest reconstruction error (E). (b) Plot of the experimentally observed peak shift (Δx) and the CS empirically determined shift (Δx_{cs}) as a function of scan rate based on CLP line scan measurements across an isolated 150 μm diameter Pt disk for comparison. (c) Plot of the optimal λ_c parameter as a function of scan rate for image reconstruction for the same four-disk sample.

from the most error, which is related to the fact that they are physically located closer together than any other disk pair and thus most prone to incorrectly being reconstructed as spatial resolution worsens at high scan speeds. Also, the "ghost" spots seen in images reconstructed from line scans measured for v_p = 121 μm s^{-1} and above are a direct result of an improperly chosen shift parameter Δx. For fast line scans without an optimized shift parameter, the locations of peaks appearing within a given line scan will not coincide with the physical location of the disks, leading the original CS reconstruction algorithm to try to (incorrectly) place disks at locations that are generally pushed away from the center of the imaging area. Consistent with the observation of increasing Δx with increasing v_p in the example line scans shown in Figure 2c, the number of ghost peaks and their distance from the center of the imaging area also increase with increasing v_p.

Qualitatively, the CS reconstruction process breaks down when the actual measurements deviate too much from the model underlying the CS reconstruction algorithm, which can happen if the noise is too high or if the measurement has a significant shift due to the high speed. To quantitatively assess the accuracy of the CS-generated SECM images, a reconstruction error was computed and plotted as a function of the CLP scan speed. This reconstruction error (E) was calculated based on differences in the locations of the disk locations from the reconstructed images to their locations in the "true image" (Figure 3b), which is obtained based on the known locations of the physical disk electrodes in the real sample (Figure 3a) and the baseline PSF. To calculate the reconstruction error, we first find a best pairing between the recovered disks and expected four disks that minimizes the sum of distances between all pairs of points, L_{pair}. Additionally, the number of missing or extra disks in the recovered image compared with the expected image, N_{diff}, is also computed. In this study, we defined reconstruction error as $E = L_{pair}/(L_{image}/2) + N_{diff}$, where L_{image} is the length of the image. This formula effectively takes into account inaccuracies in both the numbers and locations of electroactive objects. The reconstruction error can alternately be defined in a way that also accounts for variations in signal intensity, but it was not employed in this work because the position-based reconstruction error was found to be a straightforward quantity to analyze and use to identify scan rates beyond which the ability to do CS reconstruction breaks down.

Figure 3g shows how the reconstruction error changes as a function of v_p, revealing that there is a significant increase in error as v_p increases from 41 μm s^{-1} up to ≈100 μm s^{-1}. This latter speed corresponds to $Pe \approx 1$, indicating that image reconstruction based on the conventional algorithm starts to break down when entering operational regime 2 shown in Figure 2d. This result shows that CLP scan speeds cannot be much higher than the usual scan speed limit for micron-sized probes in conventional SECM when image reconstruction is based on the conventional, unmodified CS algorithm.

3.4. Image Reconstruction at Fast Scan Rates Using the Modified CS Algorithm. To overcome the limited ability of the conventional CS algorithm to tolerate line scan distortion effects at high scan speeds, the following changes to the reconstruction algorithm were implemented: First, a linear shift parameter, Δx_{cs}, was introduced into the point spread function. As with the experimental variable Δx, Δx_{cs} is a linear shift in the observed line scan curve in the direction of the scan and effectively gives a lag to the point spread function so that the signal intensity is no longer centered at the location where the signal originates. Second, λ_c was allowed to vary rather than being set as a constant as in previous studies. To view the impact of varying Δx_{cs} and λ_c on the accuracy of the reconstructed images, a two-dimensional grid search across wide ranges of Δx_{cs} and λ_c was carried out using the modified CS algorithm to reconstruct images of the four-disk sample for all probe scan rates. As a part of this grid search, all combinations of Δx_{cs} and λ_c within a wide range of candidate values were used to reconstruct images, and the reconstruction error was plotted as a function of Δx_{cs} and λ_c for each set of CLP measurements taken at a given scan speed. One example is shown in Figure 4a for imaging of the four-disk sample at v_p = 121 μm s^{-1}, for which an optimal combination of Δx_{cs} = 0.194 mm and λ_c = 0.04 is found to minimize error. From this figure, we see that a proper choice of Δx_{cs} and λ_c is essential to the reconstruction and can significantly decrease the reconstruction error compared to the baseline case where no adjustment is present (Δx_{cs} = 0.0 mm and λ_c = 0.05), corresponding to the black dot in Figure 4a. Figure 4b shows a comparison of the experimentally observed values of Δx to the

https://doi.org/10.1021/acs.analchem.1c01869
Anal. Chem. 2021, 93, 12574−12581

optimal Δx_{cs} values determined empirically by the CS algorithm to minimize reconstruction error. Overall, the CS-determined shift parameter is in very good agreement with the experimentally measured Δx up to the scan rate of 425 μm s^{-1} (Pe = 5). Similarly, Figure 4c shows the optimized λ_c parameter for CS image reconstruction that minimizes reconstruction error at the optimal shift found by the grid search. Significant increases in λ_c are needed for v_p > 100 μm s^{-1}, which is likely required to maintain accurate image reconstruction by compensating for the increase in signal-to-noise ratio, increase in FWHM, and higher asymmetry of features when imaging is carried out at probe scan rates corresponding to regime 2 of Figure 2d.

The results of Figure 4 can subsequently be used as guidelines for the selection of optimal Δx_{cs} and λ_c parameters for CS image reconstruction. From Figure 4b, the relationship between the shift parameter value that optimizes image accuracy and the CLP scan rate is as follows: Δx_{cs} (mm) = $5.0 \cdot (v_p \text{ (mm s}^{-1}))^2 + 0.8 \cdot v_p \text{ (mm s}^{-1})$. From Figure 4c, the optimal normalized sparsity coefficient λ_c should be set to be a constant λ_c = 0.05 for scan rates below 120 μm s^{-1} but is dependent on scan rates above 120 μm s^{-1} according to $\lambda_c = 0.84 \cdot v_p \text{ (mm s}^{-1}) - 0.05$. This relationship is consistent with the CS theory. Specifically, when the probe scan rate is characterized by a high Pe, the strong convection will introduce noise to our measurement, and hence, a higher λ_c is needed to suppress this noise. On the other hand, when v_p is relatively low, this particular noise does not significantly affect the quality of measurements, and hence, a fixed level of λ_c suffices.

Having determined the optimal parameters for the modified CS reconstruction algorithm, it was then used to generate images based on CLP line scan data recorded at the elevated scan speeds (v_p > 100 μm s^{-1}) that the conventional algorithm was not able to successfully reconstruct images from in Figure 3. Figure 5 shows that the modified algorithm not only is able to accurately reconstruct images from the v_p = 121 and 223 μm s^{-1} data sets but also does a decent job of recovering the four disks for v_p = 425 μm s^{-1} (Pe = 5.0). A comparison of the reconstruction error across all data sets for the conventional and modified CS algorithms is provided in Figure 5e and clearly reveals the superiority of the latter algorithm, although it should be acknowledged that there is still a slight loss in accuracy at these higher scan rates. Nonetheless, this work shows that the modified CS algorithm has enabled extension of the upper scan limit into operational regime 2 (1 < Pe < 5), effectively increasing the speed limit for the CLP by nearly an order of magnitude (i.e., from $v_p \approx 40$ μm s^{-1} up to $v_p \approx 400$ μm s^{-1}). Increasing scan speeds even further, into regime 3, results in even higher reconstruction error, and we find that even the modified CS algorithm is not able to accurately reconstruct images for Pe > 500 μm s^{-1}. At these scan speeds, we surmise that the higher signal-to-noise ratio and other distortion effects become especially problematic due to the onset of more chaotic or irregular convection cells that develop at these scan speeds.

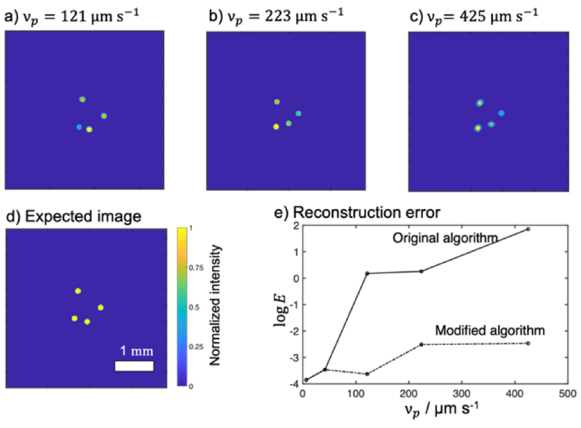

Figure 5. Compressed sensing (CS) image reconstruction based on the modified algorithm described in the text for CLP line scan data sets of the four-disk sample at scan rates of (a) 121 μm s^{-1}, (b) 224 μm s^{-1}, and (c) 425 μm s^{-1} compared with (d) true sample image. The data sets are the same as those described in the Figure 3 caption. (e) Reconstruction error at different scan rates using the modified algorithm compared with the original algorithm. The scale bar shown in (d) also applies to figures (a−c).

Implications of this work also extend beyond the CLP that was the focus of this study. It should be emphasized that the exact Pe corresponding to the transition between operational regimes 2 and 3 is expected to be highly dependent on the probe geometry and the associated hydrodynamics of that probe during scanning. The geometry of the standard CLP employed here was not at all optimized for hydrodynamics, but it is straightforward to conceive modified CLPs or alternate nonlocal probe designs that do not generate irregular flow patterns until higher Pe. Promisingly, decreasing the probe−substrate separation distance concurrently with the critical probe dimension (e.g., t_E for the CLP) also decreases Pe, suggesting that both higher spatial resolution and absolute scanning speeds are possible than those demonstrated in this work.

4. CONCLUSIONS

The development of fast SECM methods capable of imaging large areas (0.1−10's of cm^2) has the potential to enable both (i) new scientific capabilities like large-area video rate electrochemical imaging and (ii) commercial applications like high-throughput sensing, material discovery, and inline inspection tools for advanced manufacturing processes. Toward this end, fast-scanning nonlocal probe geometries such as CLPs that leverage compressed sensing for image reconstruction are highly attractive. Even though these unconventional probes and modern approaches to SECM image reconstruction are not yet commonly used today and have not been demonstrated with nanoscopic resolution, the order of magnitude increase in CLP scan speeds reported in this study is a significant step toward enabling new SECM-based science and applications.

The key advance that enabled this boost in the scan rate "speed limit" for electrochemical imaging using CLPs was a modified compressed sensing (CS) image reconstruction algorithm. By systematically analyzing the dependence of image distortion characteristics on probe scan speed for an isolated Pt disk electrode, three main operational regimes were identified and classified according to the transport characteristics of the system: (i) a diffusion-controlled regime, (ii) an intermediate regime where convection and diffusion are closely balanced, and (iii) a convection-controlled regime. At higher scan rates (high Pe), convection causes significant shifts and distortions in recorded SECM signals, and this work has shown that it is essential to compensate for these effects during the CS postprocessing. Using a modified CS algorithm that incorporates a shift parameter and sparsity coefficient, successful image

https://doi.org/10.1021/acs.analchem.1c01869
Anal. Chem. 2021, 93, 12574−12581

reconstruction of a simple four-disk sample was possible for CLP scan rates up to around 425 μm s^{-1} (Pe = 5). At even higher scan rates, successful imaging is hindered by larger distortions in scanned signals and the effectiveness of CS algorithms under high noise, although further optimization of SECM probe geometries can be expected to push the "speed limit" even further. By combining the use of faster probe scan rates with the inherently high throughput imaging capabilities of nonlocal probes like CLPs, significant gains in the areal imaging rates of SECM microscopes can be expected in the coming years.

■ ASSOCIATED CONTENT

Supporting Information

The Supporting Information is available free of charge at https://pubs.acs.org/doi/10.1021/acs.analchem.1c01869.

Definition and illustration of scan angle; example data set of line scan measurements (PDF)

■ AUTHOR INFORMATION

Corresponding Authors

John Wright − *Department of Chemical Engineering, Columbia University in the City of New York, New York, New York 10027, United States; Data Science Institute, Columbia University in the City of New York, New York, New York 10027, United States*; Email: jw2966@columbia.edu

Daniel V. Esposito − *Department of Chemical Engineering, Columbia University in the City of New York, New York, New York 10027, United States; Columbia Electrochemical Energy Center and Lenfest Center for Sustainable Energy, Columbia University in the City of New York, New York, New York 10027, United States*; orcid.org/0000-0002-0550-801X; Email: de2300@columbia.edu

Authors

Anna E. Dorfi − *Department of Chemical Engineering, Columbia University in the City of New York, New York, New York 10027, United States*

Jingkai Yan − *Department of Electrical Engineering, Columbia University in the City of New York, New York, New York 10027, United States; Data Science Institute, Columbia University in the City of New York, New York, New York 10027, United States*

Complete contact information is available at: https://pubs.acs.org/10.1021/acs.analchem.1c01869

Author Contributions

#A.E.D. and J.Y. share first authorship.

Notes

The authors declare no competing financial interest.

■ ACKNOWLEDGMENTS

The authors would like to acknowledge funding support from the National Science Foundation under Grant NSF CHE-1710400. Any opinions, findings, and conclusions or recommendations expressed in this material are those of the authors and do not necessarily reflect the views of the National Science Foundation. We would also like to thank Mariam Avagyan for helpful discussions and Daniela Fraga Alvarez for help obtaining sample photos.

■ REFERENCES

(1) Momotenko, D.; Byers, J. C.; McKelvey, K.; Kang, M.; Unwin, P. R. *ACS Nano* **2015**, *9*, 8942−8952.
(2) Kang, M.; Momotenko, D.; Page, A.; Perry, D.; Unwin, P. R. *Langmuir* **2016**, *32*, 7993−8008.
(3) Bard, A. J.; Denuault, G.; Friesner, R. A.; Dornblaser, B. C.; Tuckerman, L. S. *Anal. Chem.* **1991**, *63*, 1282−1288.
(4) Combellas, C.; Fermigier, M.; Fuchs, A.; Kanoufi, F. *Anal. Chem.* **2005**, *77*, 7966−7975.
(5) Dorfi, A. E.; Zhou, S.; West, A. C.; Wright, J.; Esposito, D. V. *ChemElectroChem* **2020**, *7*, 2424−2432.
(6) Lesch, A.; Vaske, B.; Meiners, F.; Momotenko, D.; Cortés-Salazar, F.; Girault, H. H.; Wittstock, G. *Angew. Chem. Int. Ed.* **2012**, *51*, 10413−10416.
(7) Lesch, A.; Momotenko, D.; Cortés-Salazar, F.; Wirth, I.; Tefashe, U. M.; Meiners, F.; Vaske, B.; Girault, H. H.; Wittstock, G. *J. Electroanal. Chem.* **2012**, *666*, 52−61.
(8) Lesch, A.; Momotenko, D.; Cortés-Salazar, F.; Roelfs, F.; Girault, H. H.; Wittstock, G. *Electrochim. Acta* **2013**, *110*, 30−41.
(9) O'Neil, G. D.; Kuo, H. W.; Lomax, D. N.; Wright, J.; Esposito, D. V. *Anal. Chem.* **2018**, *90*, 11531−11537.
(10) Dorfi, A. E.; Kuo, H.; Smirnova, V.; Wright, J.; Esposito, D. V. *Rev. Sci. Instrum.* **2019**, *90*, No. 083702.
(11) Sun, T.; Yu, Y.; Zacher, B. J.; Mirkin, M. V. *Angew. Chem. Int. Ed.* **2014**, *53*, 14120−14123.
(12) Sun, P.; Mirkin, M. V. *Anal. Chem.* **2006**, *78*, 6526−6534.
(13) Bentley, C. L.; Edmondson, J.; Meloni, G. N.; Perry, D.; Shkirskiy, V.; Unwin, P. R. *Anal. Chem.* **2019**, *91*, 84.
(14) Kuss, S.; Kuss, C.; Trinh, D.; Schougaard, S. B.; Mauzeroll, J. *Electrochim. Acta* **2013**, *110*, 42−48.
(15) Kuss, S.; Trinh, D.; Danis, L.; Mauzeroll, J. *Anal. Chem.* **2015**, *87*, 8096−8101.
(16) Kuss, S.; Trinh, D.; Mauzeroll, J. *Anal. Chem.* **2015**, *87*, 8102−8106.
(17) Kiss, A.; Nagy, G. *Electrochim. Acta* **2015**, *163*, 303−309.
(18) Kiss, A.; Nagy, G. *Electroanalysis* **2015**, *27*, 587−590.
(19) Momotenko, D.; McKelvey, K.; Kang, M.; Meloni, G. N.; Unwin, P. R. *Anal. Chem.* **2016**, *88*, 2838−2846.
(20) Lee, C.; Wipf, D. O.; Bard, A. J.; Bartels, K.; Bovik, A. C. *Anal. Chem.* **1991**, *63*, 2442−2447.
(21) Lustig, M.; Donoho, D. L.; Santos, J. M.; Pauly, J. M. *IEEE Signal Process. Mag.* **2008**, *25*, 72−82.
(22) Soltanian-Zadeh, H.; Windham, J. P.; Peck, D. J. *IEEE Trans. Med. Imaging* **1996**, *15*, 749−767.
(23) Potter, L. C.; Ertin, E.; Parker, J. T.; Çetin, M. *Proc. IEEE* **2010**, *98*, 1006−1020.
(24) Brady, D. J.; Choi, K.; Marks, D. L.; Horisaki, R.; Lim, S. *Opt. Express* **2009**, *17*, 13040.
(25) Jerri, A. J. *Proc. IEEE* **1977**, *65*, 1565−1596.
(26) Donoho, D. L. *IEEE Trans. Inf. Theory* **2006**, *52*, 1289−1306.
(27) Candes, E. J.; Wakin, M. B. *IEEE Signal Process. Mag.* **2008**, *25*, 21−30.
(28) West, A. C. *Electrochemistry and Electrochemical Engineering. An Introduction*; CreateSpace Independent Publishing Platform: 2012.
(29) Wehmeyer, K. R.; Deakin, M. R.; Wightman, R. M. *Anal. Chem.* **1985**, *57*, 1913−1916.
(30) Kuo, H.-w. clpsecm/clpsecm_imaging: Recovery SECM image from continuous-line probe (CLP) scans.
(31) Candes, E. J.; Wakin, M. B.; Boyd, S. P. *J. Fourier Anal. Appl.* **2008**, *14*, 877−905.
(32) Bard, A. J.; Mirkin, M. V.; Unwin, P. R.; Wipf, D. O. *J. Phys. Chem.* **1992**, *96*, 1861−1868.
(33) Kuo, H.-W.; Dorfi, A. E.; Esposito, D. V.; Wright, J. N. Compressed Sensing Microscopy with Scanning Line Probes. *arXiv:1909.12342* 2019, 1−15.